Frontiers of Information Technology & Electronic Engineering
www.jzus.zju.edu.cn; engineering.cae.cn; www.springerlink.com
ISSN 2095-9184 (print); ISSN 2095-9230 (online)
E-mail: jzus@zju.edu.cn



# A convolutional neural network based approach to sea clutter suppression for small boat detection

Guan-qing LI[†], Zhi-yong SONG[†‡], Qiang FU

*National Key Laboratory of Science and Technology on ATR, College of Electronic Science and Technology, National University of Defense Technology, Changsha 410073, China*

[†]E-mail: liguanqing09@nudt.edu.cn; songzhiyong08@nudt.edu.cn

Received Sept. 25, 2019; Revision accepted Mar. 22, 2020; Crosschecked May 18, 2020

**Abstract:** Current methods for radar target detection usually work on the basis of high signal-to-clutter ratios. In this paper we propose a novel convolutional neural network based dual-activated clutter suppression algorithm, to solve the problem caused by low signal-to-clutter ratios in actual situations on the sea surface. Dual activation has two steps. First, we multiply the activated weights of the last dense layer with the activated feature maps from the upsample layer. Through this, we can obtain the class activation maps (CAMs), which correspond to the positive region of the sea clutter. Second, we obtain the suppression coefficients by mapping the CAM inversely to the sea clutter spectrum. Then, we obtain the activated range-Doppler maps by multiplying the coefficients with the raw range-Doppler maps. In addition, we propose a sampling-based data augmentation method and an effective multiclass coding method to improve the prediction accuracy. Measurement on real datasets verified the effectiveness of the proposed method.

**Key words:** Convolutional neural networks; Class activation map; Short-time Fourier transform; Small target detection; Sea clutter suppression

https://doi.org/10.1631/FITEE.1900523 **CLC number:** TN957.51

## 1 Introduction

When radar tries to detect small boats on the sea surface, it is necessary to design suitable detectors or use effective sea clutter suppression methods. These detection methods are all based on the understanding of sea clutter characteristics, including amplitude distribution, texture correlation, and Doppler spectrum.

For many modern high-resolution radar systems, the Rayleigh distribution density model underestimates the tails of the measured sea clutter density (Shnidman, 1999). Trunk and George (1970) proposed the log-normal distribution; however, sometimes the tail of the probability density function (PDF) estimated by log-normal is overfitting. Sekine et al. (1983) proposed the Weibull distribution, of which PDF lies between Rayleigh and log-normal distributions, and Farina et al. (1997) used it for modeling sea clutter. Ward (1981) used composite modulation to model high-resolution radar sea clutter and proposed a *K*-distribution model. Greco et al. (2006) proposed a generalized *K*-distribution model to estimate the clutter amplitude distributions based on ice multiparameter imaging X-band (IPIX) radar clutter data. There are also models which can explicitly model sea spikes including the KA- and KK-distributions, while others such as the Pareto-distribution just model the longer tails in the presence of spikes (Rosenberg et al., 2019).

The correlation of the texture can be characterized by temporal correlation and spatial correlation. Farina et al. (1997) and Greco et al. (2006) analyzed the temporal correlation of clutter in the IPIX radar

‡ Corresponding author
ORCID: Guan-qing LI, https://orcid.org/0000-0002-9789-8931; Zhi-yong SONG, https://orcid.org/0000-0002-3833-0510
© Zhejiang University and Springer-Verlag GmbH Germany, part of Springer Nature 2020

sea clutter data. Greco et al. (2006) mentioned that the correlation times of the sea clutter speckle component and the modulation component are about 10 ms and 1 s, respectively. Watts and Ward (1987) analyzed the clutter spatial correlation between multiple range bins with measured sea clutter data and showed the correlation related to wind speed and radar sight (Watts, 1996). The clutter correlation function and the clutter Doppler spectrum are Fourier transform pairs. Walker (2000, 2001) analyzed the characteristics of the clutter Doppler spectrum at low grazing angles based on measurement data and proposed a theoretical model of the Doppler spectrum. Lamont-Smith (2008) studied the sea clutter Doppler spectrum characteristics of the low grazing angle radar at different observation angles. Ritchie et al. (2016) analyzed the sea clutter texture correlation and the characteristics of the Doppler spectrum based on the *K*-distribution model, using data from the NetRAD radar. Here, the Doppler spectrum analysis is based on a short-time Fourier transform, where each spectrum is taken over a period that is of the order of 128 ms.

Based on the study of sea clutter characteristics, researchers have designed a variety of radar target detectors to improve the signal-to-noise ratio (SNR). Detectors including Neyman Pearson (NP) (Gini et al., 2002), generalized likelihood ratio test (GLRT) (Gini et al., 2000; Conte and de Maio, 2004; Hao et al., 2014), generalized likelihood ratio test linear-threshold detector (GLRT-LTD) (Sangston et al., 2012; Shui and Liu, 2016; Shi et al., 2019), and adaptive normalized matched filter (ANMF) are used for detection (de Maio et al., 2005; Greco et al., 2010; Shui and Shi, 2012; McDonald MK and Cerutti-Maori, 2016). For *K*-distribution and KK-distribution sea clutter, optical *K*-distribution detector (OKD) usually has better performance (Jay et al., 2002; Dong, 2012; Weinberg, 2012). McDonald AM et al. (2010) assumed that the clutter obeys the *K* distribution in both time and frequency domains, and then analyzed the detection performance of the radar under the *K*-distribution clutter from the perspective of frequency-domain detection. The premise of these detectors is that the sea clutter and the target are separable enough in the time or Doppler domain (Herselman and de Wind, 2008). For a small boat within energetic sea clutter, the premise above is no longer satisfied, resulting in a decrease in detection performance.

Another widely used radar small target detection method is sea clutter suppression, which can be divided into two major categories (Lv and Zhou, 2019). The first category includes the time-domain cancellation method, which operates by using the frequency or power spectrum to estimate the relevant parameters and reconstructing the sea clutter in the time domain. Then there is subtraction from the echo signal to achieve clutter suppression, which is represented by the root loop cancellation method (Wu et al., 2010; Guan et al., 2012; Zhao JR et al., 2019). The second category is based on the subspace projection class method by obtaining the clutter subspace (Gini et al., 2002; Liu J et al., 2012). Then it suppresses sea clutter through subspace projection, achieving a suppression of 15–20 dB. However, the two categories of methods above are ineffective when the target and clutter cannot be divided in the time or frequency domain. Furthermore, in the case of low SNR, the target subspace and clutter subspace do not meet the orthogonality condition.

To solve these difficulties, methods based on time-frequency analysis and sparse Fourier transform have been proposed in recent years. Yasotharan and Thayaparan (2006) analyzed the time-frequency characteristics of sea clutter and used time-frequency filtering to suppress sea clutter. Wang WP et al. (2019) proposed an improved time-frequency filtering method based on the time-spectrum energy distribution. There are also methods for target detection using time-frequency (TF) images with machine learning methods such as support vector machines (SVMs) (Li Y et al., 2017; Li YZ et al., 2019) and artificial neural networks (ANNs) (Del-Rey-Maestre et al., 2018; Fernández and Vidal, 2018; Zhao JF et al., 2019).

Gaze observation radar greatly prolongs the time of observing the target and improves the performance of detecting the small target in the clutter background. However, this gaze observation mode will result in a lot of time and Doppler information, and the machine learning methods above cannot meet real-time processing requirements. Sparse Fourier transform (SFT) techniques are widely used in radar detection to reduce calculation costs (Hassanieh et al., 2012; Gilbert et al., 2014; Wang SG et al., 2016; Pang et al., 2018). Yu et al. (2019) proposed adaptive moving target indication with adaptive dual-threshold sparse Fourier

transform (AMTI-ADT-SFT) for radar small boat detection. The sparsity of the SFT-based method still relies on manual design, and is not easy to obtain. The number of false alarms needs to be further reduced for practical applications.

With the development of deep learning (Khan et al., 2019), many works for radar target detection via convolutional neural networks (CNNs) have sprung up (Wang C et al., 2017; Angelov et al., 2018; Kong et al., 2018; Guo et al., 2019; Zhang RY and Cao, 2019). Wang L et al. (2019) proposed a CNN-based coincidence detection process with simulated radar data, and obtained better performance than traditional constant false alarm rate (CFAR) detectors. In addition, CNNs can be used for high-dimensional sea clutter feature extraction (Liu NB et al., 2019), sea clutter reflectivity estimation (Ma et al., 2020), and spectrum sensing (Liu C et al., 2019). Furthermore, Adolfsson and Rahm (2018) used ResNet to detect long-distance boats with airborne radar data. Zhang L et al. (2018) used faster R-CNN for boat detection with time-frequency images collected by high-frequency surface wave radar (HFSWR). Su et al. (2019) used GoogLeNet to classify sea states and polarization states with IPIX time-frequency images.

There have been many radar target detection methods based on CNNs as mentioned above. However, for data recorded under very complex sea conditions such as Council for Scientific and Industrial Research (CSIR) radar data (Herselman et al., 2008), CNNs need to overcome some difficulties to find the target. First, the sea clutter and the target sometimes are not separable in the time or Doppler domain, and the detection performance of conventional detection methods will decrease. Second, there are not enough labeled data since the boat appears only in several range bins, although sea clutter images may be sufficient. Also, the network should be interpretable to understand the physical meaning of the features learned by the network model. The conventional one-hot coding method for labeling is not accurate enough in this scenario, because the boat usually appears with the waves. Finally, we must verify whether the detection speed of the model meets the requirements, which is beneficial to the practical application of the algorithm.

Zhou et al. (2016) showed that replacing fully connected layers with an average pooling layer can help generate coarse class activation maps (CAMs) that highlight task-relevant regions. The basic idea of the CAM method is to remove the global average pooling (GAP) layer and treat the model as a fully convolutional architecture (Long et al., 2015). CAM can be used for classifying artistic media (Yang and Min, 2019), CT images (Lei et al., 2020), person re-identification (Liu S et al., 2020), saliency prediction of human visual attention (Mahdi and Qin, 2019), etc.

Based on research on CAMs, time-frequency analysis, radar CFAR detection, and sea clutter suppression methods, we propose a dual-activation CNN based clutter suppression (DA-CCS) algorithm for radar small boat detection on the sea surface. To the best of our knowledge, it is the first time that sea clutter has been suppressed by CNNs. Dual activation holds two steps in total. First, we multiply the activated weights of the last dense layer with the activated feature maps from the upsample layer. Through this, we can obtain CAMs, which correspond to the positive region of sea clutter. Second, we obtain the suppression coefficients by mapping the CAM inversely to the sea clutter spectrum. Then, we obtain the activated range-Doppler maps by multiplying the coefficients with the raw range-Doppler maps. In addition, we propose a sampling-based data augmentation method and an effective multiclass coding method to improve the prediction accuracy.

## 2 Theories

### 2.1 Data preprocessing

#### 2.1.1 Time-frequency analysis

Let $\boldsymbol{D}\in\mathbb{C}^{P\times R}$ be the complex matrix of radar raw echoes, where $P$ and $R$ are the total numbers of pulses and range bins, respectively. Take the columns $\boldsymbol{D}_r\in\mathbb{C}^{P\times 1}$ ($1\le r\le R$) from matrix $\boldsymbol{D}$. $\boldsymbol{D}_r$ represents the radar echoes from the $r^{\text{th}}$ range bin. Let $F_{\text{prf}}$ be the pulse repetition frequency, and time for $\boldsymbol{D}_r$ is $F_{\text{prf}}^{-1}\cdot P$ seconds.

The result of short-time Fourier transform (STFT) for radar echoes can be represented as

$$X_r[k,n]=\sum_{m=0}^{N-1}D_r[m+n]\cdot w[N-1-m]\cdot \mathrm{e}^{-\mathrm{j}\frac{2k\pi}{N}m}, \quad (1)$$

where $X_r[k, n]$ represents the result of STFT for the $r^{\text{th}}$ range bin with Doppler $k$ and time $n$, $\boldsymbol{w}\in\mathbb{R}^{N\times 1}$ is the window function, $1\le k\le N-1$, $0\le n\le P-N-1$, $N$ is the length of the window, $X_r[k, n]\in\mathbb{C}$, and $\boldsymbol{X}_r[:, n]\in\mathbb{C}^{N\times 1}$.

To reduce calculation costs, we set an interval $n_l$ between $X_r[k, n]$ and $X_r[k, n+1]$. Then the new result of STFT can be represented as

$$\tilde{X}_r[k,n]=\sum_{m=0}^{N-1}D_r[m+n_l n]\cdot w[N-1-m]\cdot \mathrm{e}^{-\mathrm{j}\frac{2k\pi}{N}m}, \quad (2)$$

where $0\le n\le \tilde{P}-1$, $\tilde{\boldsymbol{X}}_r\in\mathbb{C}^{N\times\tilde{P}}$, and $\tilde{P}=\lfloor P/n_l\rfloor$ ($\lfloor\cdot\rfloor$ is the downward integer function). In this way, the calculation costs have been reduced by $(n_l-1)/n_l$. We take $K$ values near the zero frequency as $\boldsymbol{M}_r\in\mathbb{C}^{K\times\tilde{P}}$ from $\tilde{\boldsymbol{X}}_r$. Normalize $\boldsymbol{M}_r$ as follows:

$$\tilde{\boldsymbol{M}}_r=10\lg\left(\frac{\boldsymbol{M}_r\boldsymbol{M}_r^*}{\max(\boldsymbol{M}_r\boldsymbol{M}_r^*)}\right), \quad (3)$$

where function $\max(\cdot)$ will choose the largest value of the matrix and $\tilde{\boldsymbol{M}}_r\in\mathbb{R}^{K\times\tilde{P}}$. The resolution of the Doppler frequency can be represented as

$$\Delta f=\frac{F_{\text{prf}}}{N}. \quad (4)$$

Make pseudo color transformation $T_i[\cdot]$ ($i$=1, 2, 3) with matrix $\tilde{\boldsymbol{M}}_r$. Then we can obtain the time-frequency image $\boldsymbol{I}_r\in\mathbb{N}^{H\times W\times 3}$ for the $r^{\text{th}}$ range bin, where $0\le I_r[h, w, i]\le 255$. The Doppler frequency ranges from $-K\Delta f/2$ to $K\Delta f/2$. Matrix $\boldsymbol{I}_r$ can be represented as

$$\boldsymbol{I}_r=T_i[\tilde{\boldsymbol{M}}_r]. \quad (5)$$

### 2.1.2 Data augmentation

Dada augmentation is an effective approach for dealing with limited training data (Cui et al., 2015). The method can be represented as the mapping

$$\phi:\mathcal{S}\mapsto\mathcal{T}, \quad (6)$$

where $S$ is the original dataset and $\mathcal{T}$ is the newly added dataset transformed by the mapping $\phi(\cdot)$. Then the total training set can be expressed as

$$\widetilde{\mathcal{S}}=\mathcal{S}\cup\mathcal{T}. \quad (7)$$

Note that the image $\boldsymbol{I}$ from the original training set and the mapped images $\phi(\boldsymbol{I})$ belong to the same class.

We make left-right and up-down transforms for image $I(x, y, c)$, which contains $W$ and $H$ pixels in the $x$- and $y$-coordinate, respectively. The left-right and up-down transforms can be expressed as

$$I_{\text{LR}}(x,y,c)=I(W-x,y,c), \quad (8)$$

$$I_{\text{UD}}(x,y,c)=I(x,H-y,c). \quad (9)$$

Usually, we can obtain only one time-frequency image from radar echo data over a period of time. Then the other time-frequency image is obtained from the next section of the data. The length of data should not be too short; otherwise, it will be difficult to extract effective time-frequency characteristics. Inspired by the average periodic graph method for power spectrum estimation, we partially overlap the two sections of data to obtain more time-frequency images. We can obtain more images by sampling with $\boldsymbol{X}_r$ without decreasing the time and frequency resolutions. Compared with the translation-based method, the sampling-based method has more distribution information. Although the images have redundancy, the method is still very effective for training a deep network. In theory, the total number of images generated by this method is $S$ times that of the original image datasets:

$$S=\left\lfloor\frac{1}{1-\xi}\right\rfloor,\ 0<\xi<1, \quad (10)$$

where $\xi$ is the overlap rate between the two overlapped TF images.

### 2.1.3 Labeling with multiple labels

Most of the algorithms for classification are calculated with the metrics in the vector space, to make the points not equidistant (Jafarzadehpour et al.,

2019). One-hot encoding makes the distance calculation between features more reasonable, so it has been widely used in deep learning.

In the situation of radar small boat detection with energetic sea clutter, a boat usually appears simultaneously with sea clutter in time-frequency images. Therefore, one-hot coding is not accurate. It uses "01" to represent "sea clutter" and "10" to represent "sea clutter+boat." It is also not accurate to use three labels "0," "1," "2."

$$\tilde{\phi}:\mathcal{T}\mapsto\{[10],[01],[11]\}. \tag{11}$$

We propose a new encoding method with multiple labels as shown above. "01" means that there is only sea clutter, "11" represents that there are sea clutter and a boat at the same time, and "10" means that there is only a boat.

## 2.2 DA-CCS algorithm for boat detection

In this study, we propose a dual-activation CNN based sea clutter suppression (DA-CCS) algorithm for small boat detection on the sea surface. The procedure of the algorithm is shown in Fig. 1. "TF images" represent the input images, and "CAM for boat" represents the class activation map. The VGG model has five blocks, which own several convolutional layers and maxpooling layers. The weights of "VGG 16" trained by the ImageNet dataset are fixed. Feature maps from the fourth block are selected as the training and testing datasets. We add several layers as the "Add_Model," which is trainable.

### 2.2.1 CNN forward-propagation

We add Conv2D, UpSampling2D, GlobalAveragePooling2D, and a Dense layer for the classification task. To obtain the localization of the target, we add a Conv2D layer for the last convolution block with an output $\boldsymbol{F}^{\text{vgg}}\in\mathbb{R}^{n_c\times n_c\times k_c}$, where $(n_c, n_c)$ is the size of the feature map and $k_c$ is the kernel depth. The output of the convolutional layer sized $(s_c, s_c, k_c)$ from "Add_Model" can be represented as

$$F_{i,j,c}^{(c)}=\sum_{p=0}^{s_c}\sum_{q=0}^{s_c}\left(\sum_{c'=1}^{k_c}F_{i+p,j+q,c'}^{\text{vgg}}k_{p,q,c}^{(c)}\right), \tag{12}$$

where $k_{p,q,c}^{(c)}$ represents the convolutional kernel. Then we use the bilinear interpolation with kernel size $(k_\text{u}, k_\text{u})$ at the upsample layer, and the results can be represented as

$$\begin{aligned}F_{i+p,j+q,c}^{(\text{u2})}=&(k_\text{u}-p)(k_\text{u}-q)F_{i,j,c}^{(\text{u1})}+(k_\text{u}-p)qF_{i,j+k_\text{u},c}^{(\text{u1})}\\&+p(k_\text{u}-q)F_{i+k_\text{u},j,c}^{(\text{u1})}+pqF_{i+k_\text{u},j+k_\text{u},c}^{(\text{u1})},\end{aligned} \tag{13}$$

where $0\le p,\ q\le k_\text{u}-1,\ 0\le i,\ j\le k_\text{u}n_c-1$, and $F_{k_\text{u}i,k_\text{u}j,c}^{(\text{u1})}=F_{i,j,c}^{(c)},\ 0\le c\le k_c$.

The global average pooling layer transforms the feature map of each kernel into one value, and the result is

$$F_k^{(g)}=\frac{1}{Z}\sum_{i=1}^{n_ck_\text{u}}\sum_{j=1}^{n_ck_\text{u}}F_{i,j,k}^{(\text{u2})},\ k=1,2,\cdots,k_c, \tag{14}$$

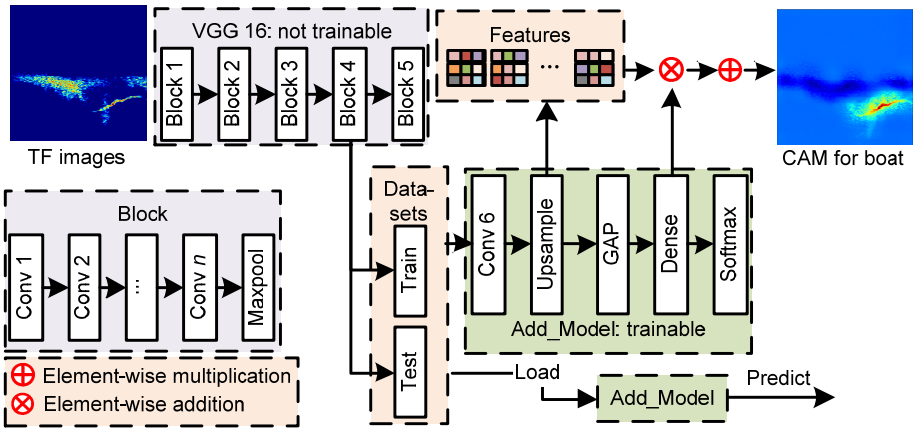



**Fig. 1 Flowchart of radar small target detection based on the dual-activation CNN based sea clutter suppression algorithm (TF: time-frequency; CAM: class activation map)**

where $Z=\sum_{i=1}^{n_c k_u}\sum_{j=1}^{n_c k_u}1$, $0\le i,\ j\le k_u n_c$, $\boldsymbol{F}^{(g)}\in\mathbb{R}^{1\times 1\times k_c}$, and $(k_u n_c, k_u n_c)$ is the size of the input TF image.

Let $\boldsymbol{w}\in\mathbb{R}^{k_d\times 2}$ be the parameters of the dense layer. $w_i^c$ represents the importance of the $i^{\text{th}}$ feature map $F_g(i)$, for the network's final prediction score $y_{c_}$. The "sigmoid" nonlinear activation function can be expressed as

$$y_{c_}=\left(1+\exp\left(-\sum_{i=1}^{k_d}w_i^c F_g(i)\right)\right)^{-1}, \tag{15}$$

where $y_{c_}\in[0, 1]$.

2.2.2 CNN back-propagation

We use the cross entropy loss as the objective function. The loss can be represented as

$$J(y_{_},y)=-\sum_{c=1}^{C}y_c\lg(y_{c_}), \tag{16}$$

where $C$ represents the total number of classes, $y_c$ means the expected output, and $y_{c_}$ indicates the predicted output of the "Softmax" layer.

According to Eqs. (14) and (15) and the chain rule for derivative

$$\frac{\partial J(y_{_},y)}{\partial w_i^c}=F_g(i)(1-y_{c_})(\ln 10)^{-1}, \tag{17}$$

the iterative solution process of the dense layer's parameter $\boldsymbol{w}$ is

$$(w_i^c)_{\text{step}+1}=(w_i^c)_{\text{step}}-\eta\frac{\partial J(y_{_},y)}{\partial w_i^c}. \tag{18}$$

2.2.3 Activating CNN features

Through resizing the input image and the results of Eq. (13), $\boldsymbol{F}_{u2}$ will have the same size as the input image. Define the class activation map $\boldsymbol{C}_r\in\mathbb{R}^{W\times H}$ for image $\boldsymbol{I}_r$ as follows:

$$\boldsymbol{C}_r=\sum_{k=0}^{k_d-1}w_k^1\boldsymbol{F}_{u2}(i,j,k),\ 1\le i\le W, 1\le j\le H, \tag{19}$$

where $H=W=n_c k_u$ and $k_d=512$.

We can obtain the hot-map by visualizing $\boldsymbol{C}_r$. The map shows the important region for predicting the image into "sea clutter" since label "01" represents "sea clutter."

2.2.4 Activating the Doppler spectrum

Activating the Doppler spectrum of sea clutter is the most significant innovation of the DA-CCS algorithm. Let $\boldsymbol{O}\in\mathbb{C}^{K\times R\times L}$ represent the range-Doppler maps of matrix $\boldsymbol{D}\in\mathbb{C}^{P\times R}$. There are $L$ range-Doppler maps in total, where $L=\lfloor P/N\rfloor$. Let

$$O_l[k,r]=M_r[k,\tilde{l}], \tag{20}$$

where $0\le k\le K-1$, $0\le r\le R-1$, and $\tilde{l}=\lfloor N_l/n_l\rfloor$.

We resize $\boldsymbol{C}_r$ to size $(K,\ \tilde{P})$ by bilinear interpolation mentioned in Eq. (13), where $\tilde{P}=\lfloor P/n_l\rfloor$. Normalize $\boldsymbol{C}_r$ into $\tilde{\boldsymbol{C}}_r$, where $0\le\tilde{C}_r[k,p]\le 1$. For CAM, the reverse map is again a negation of the reference attention map, and the maximum point will not be changed by the element-wise multiplication. Then we can obtain the activated time-frequency spectrum $\hat{\boldsymbol{M}}_r\in\mathbb{R}^{K\times\tilde{P}}$:

$$\hat{M}_r[k,p]=\tilde{C}_r[k,p]\tilde{M}_r[k,p]+\alpha_r, \tag{21}$$

where $\tilde{M}_r[k,p]\le 0$, $0\le p\le\tilde{P}-1$, and $\alpha_r$ is the conversion vector caused by normalization in Eq. (3):

$$\alpha_r=10\lg\max(\boldsymbol{M}_r\boldsymbol{M}_r^*). \tag{22}$$

According to Eqs. (20) and (21), the activated range-Doppler map can be represented as

$$\hat{O}_l[k,r]=\hat{M}_r[k,\tilde{l}], \tag{23}$$

where $0\le k\le K-1$, $0\le r\le R-1$, $\tilde{l}=\lfloor N_l/n_l\rfloor$, and $\hat{\boldsymbol{O}}\in\mathbb{C}^{K\times R\times L}$ represents range-Doppler maps after sea clutter suppression.

2.2.5 Detection based on CFAR

The procedure for traditional radar target detection is shown as Fig. 2.

As shown in Fig. 3, our method's procedure is similar to that of traditional methods. However, the clutter distribution in the range-Doppler spectrum after clutter suppression is unknown, making it difficult to control the false alarm rate with unknown clutter. We use the kernel density estimation method to solve this problem. For one-dimensional data, the estimated PDF can be represented as

$$\hat{f}(x)=\frac{1}{NB}\sum_{i=1}^{N}K\left(\frac{x-x_i}{B}\right), \tag{24}$$

where $K(x)=\mathrm{e}^{-x^2/2}/\sqrt{2\pi}$ and $B$ represents the bandwidth. Integrating the estimated PDF, the expression of the distribution function $\hat{F}(x)$ can be obtained:

$$\hat{F}(x)=\int_{-\infty}^{x}\frac{1}{NB}\sum_{i=1}^{N}K\left(\frac{t-t_i}{B}\right)\mathrm{d}t=\frac{1}{N}\sum_{i=1}^{N}\Phi\left(\frac{x-x_i}{B}\right). \tag{25}$$

Assuming the false alarm rate equal to $P_{\mathrm{fa}}$, the threshold $T$ can be obtained as

$$T=\hat{F}^{-1}(1-P_{\mathrm{fa}}). \tag{26}$$

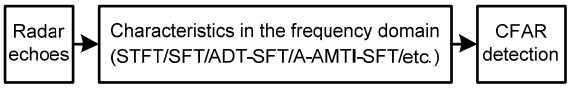



**Fig. 2 Flowchart of radar target detection based on traditional methods**

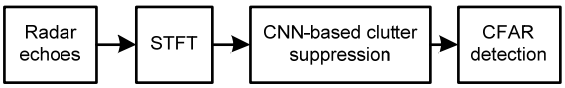



**Fig. 3 Flowchart of radar small target detection based on the DA-CCS sea clutter suppression algorithm**

## 3 Experiments and analysis of results

### 3.1 Data preprocessing

3.1.1 Datasets

Datasets used in this study are open access data recorded by radar located in South Africa. The transmitting frequency of the radar is 6.9 or 9 GHz. The pulse repetition frequency is 2.5 or 5 kHz. The range resolution of the radar is 15 m. The small boat sized 3–5 m is located via a global positioning system (GPS).

Several typical scenarios are chosen to verify the effectiveness of the proposed detection algorithm (Table 1). All of the data for training have the same Tx frequency and pulse repetition rate. The distance between the boat and the radar is between 3200 and 3800 m. Dataset TFC17002 is used for verifying the detection performance of the algorithm, which has the same Tx frequency and pulse repetition frequency as the training data. The other testing datasets are used to verify the algorithm's robustness for the Tx frequency, pulse repetition frequency, and the distance between the boat and the radar.

The signal-to-clutter ratio (SCR) of the data is calculated as follows:

$$\mathrm{SCR}=10\lg\left(\frac{\sum\left|D_{rp}D_{rp}^{*}\right|\mathrm{d}s_0}{\frac{1}{2r_1}\sum_{n}\sum\left|D_{rp}D_{rp}^{*}\right|\mathrm{d}s_n}\right), \tag{27}$$

where $\boldsymbol{D}\in\mathbb{C}^{P\times R}$ is the complex matrix of radar raw echoes, and $P$ and $R$ are the total numbers of pulses and range bins, respectively. $\sum(\cdot)\mathrm{d}s$ is the integral along the curve of the boat's trace located by the GPS.

**Table 1 Typical scenarios of the datasets**

| Data | Serial number | Tx frequency (GHz) | Pulse repetition frequency (kHz) | Target location (m) | Time (s) |
|---|---|---|---|---|---|
| Training data | TFC15001 | 9 | 5 | 3200–3400 | 0–53.86 |
| | TFC15004 | 9 | 5 | 3200–3400 | 0–13.47 |
| | ⋮ | 9 | 5 | 3200–3800 | ⋮ |
| | TFC15022 | 9 | 5 | 3200–3300 | 40.40–80.80 |
| Testing data | TFC17002 | 9 | 5 | 3300–3500 | 0–53.86 |
| | TFC15038 | 9 | 5 | 6900–7100 | 0–53.86 |
| | TFC15023 | 9 | 2.5 | 3300–3500 | 0–53.86 |
| | TFA17014 | 6.9 | 5 | 6800–6900 | 0–53.86 |

$s_n$ represents the curve obtained by shifting $n$ range bins for the trace. The range of $n$ is

$$n \in [r - r_0 - r_1, r - r_0 - 1] \cup [r + r_0 + 1, r + r_0 + r_1], \quad (28)$$

where $r$ represents the index of the range bin where the boat is at the moment. $r_0$=2 is the number of the protected cells, and $r_1$=4 is the number of cells under test (CUT).

According to Eq. (27), the SCRs of Figs. 4a and 4b are −6.36 and 3.61 dB, respectively. We show the range-Doppler maps of the two datasets in Fig. 5. The spectra of the target and sea clutter are aliased. Low SCR and aliased spectra make it difficult to efficiently detect the target for traditional detection methods.

### 3.1.2 Time-frequency analysis

We use the STFT to extract time-frequency information. It is obtained by making Fourier transform for a short-time signal in the neighborhood of $t_0$.

As an estimate for the spectrum component at time $t_0$, STFT accurately reflects the spectrum for the current time. In Ritchie et al. (2016), the Doppler spectrum analysis was taken over a period of 128 ms. Here, we set the length of window $N$ equal to 2048, to obtain a high-resolution sea clutter time-frequency map.

It can be seen from Fig. 6 that the sea clutter and the target move in opposite directions, and the Doppler spectrum of the sea clutter is planar, distributed mainly at 0–200 Hz. The boat's time-frequency spectrum is roughly a curve around −200 Hz. Within 10–20 s, the boat appears in the 20th and 21st range bins; within 20–30 s, the boat appears in the 21st and 22nd range bins; within 30–40 s, the boat appears in the 22nd and 23rd range bins.

### 3.1.3 Data augmentation and labeling

We make STFT for the training datasets and obtain 406 TF images which contain "boat" according to Eq. (2) and the GPS information. The number of images is not enough for training the deep network. We use the data augmentation method proposed in Section 2.1.2 to produce more images for training.

Fig. 7a presents the original image. Figs. 7b and 7c present images via left-right and up-down flipping according to Eqs. (8) and (9), respectively. Fig. 7d is the result of the sampling-based data augmentation method, according to Eq. (10), where $n_l$=64, $P$=67 334, $\xi$=0.8. The images obtained by the sampling-based method have more distribution information than the images obtained by shifting the original image. There are notable differences for time-frequency images with different ranges of the SCR. It is also an effective data augmentation method for deep learning. Figs. 7e and 7f present the results of setting the SNR within [−40, 0] and [−70, 0] dB, respectively.

We propose the labeling method in Section 2.1.3 to add labels for the TF images. "01" indicates that there is only sea clutter in the TF image. In Fig. 8b, the boat appears in the image, but the sea clutter is strong and its spectrum is aliased with the target's

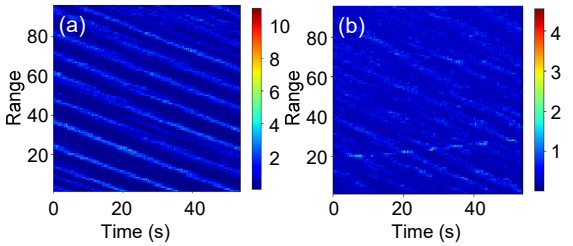



**Fig. 4 Range-pulse images for datasets TFC15001 and TFC15038: (a) the target is completely covered by sea clutter; (b) the trace of the target can be observed**

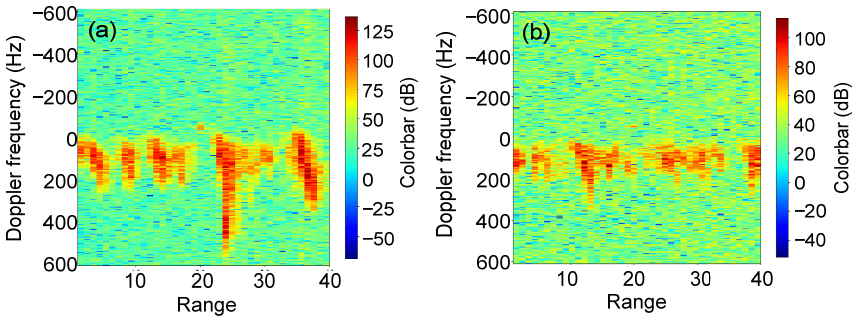



**Fig. 5 Range-Doppler maps for datasets TFC15001 (a) and TFC15038 (b)**

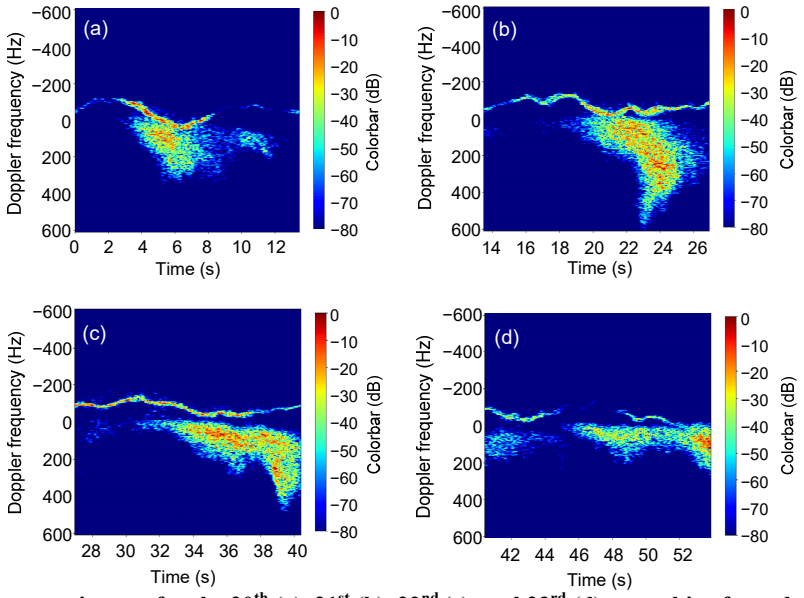



**Fig. 6 Time-frequency images for the 20th (a), 21st (b), 22nd (c), and 23rd (d) range bins from dataset TFC15001**

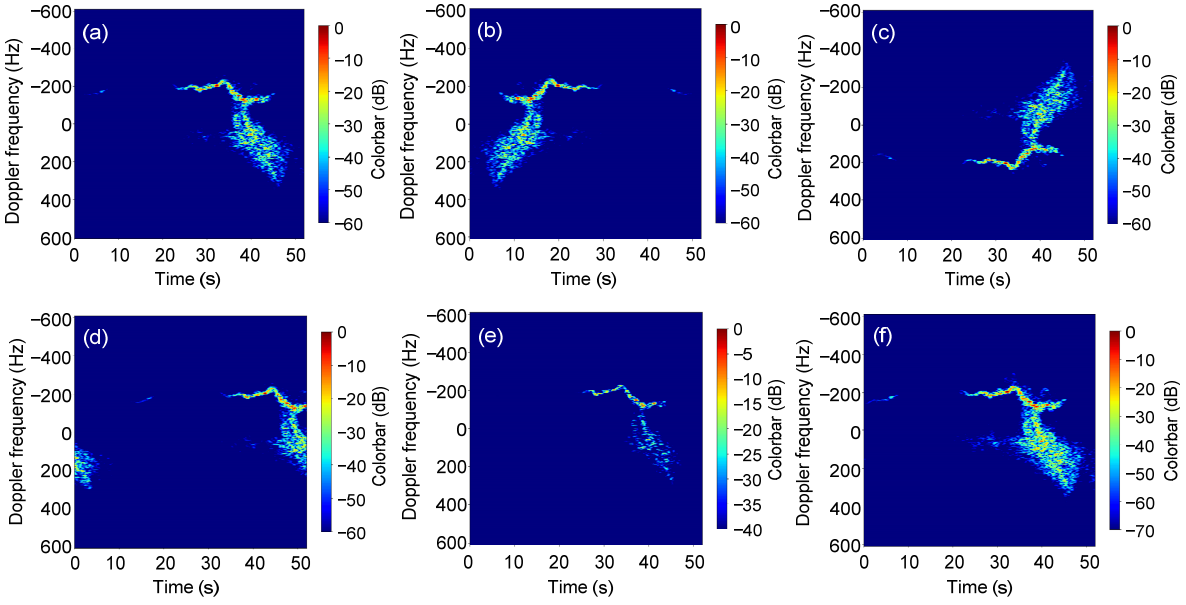



**Fig. 7 Time-frequency images via data augmentation: (a) original image; (b) image via left-right flipping; (c) image via up-down flipping; (d) result of the sampling-based data augmentation method; (e) result of setting the SNR within [−40, 0] dB; (f) result of setting the SNR within [−70, 0] dB**

spectrum. In Fig. 8c, the sea clutter is not strong enough. Then we label the image as "10." This rarely happens, though.

### 3.2 Training and testing procedures

We design a two-stage architecture for training and testing. First, we load the parameters of the VGG 16 network as shown in Fig. 1. The TF images with

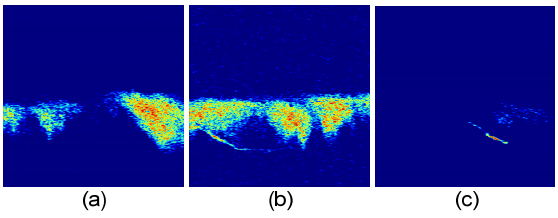



**Fig. 8 Results of labeling: (a) label "01;" (b) label "11;" (c) label "10"**

size (800, 800, 3) are resized to (224, 224, 3). The output of the fourth block sized (28, 28, 512) is the input of the next stage network (Fig. 9).

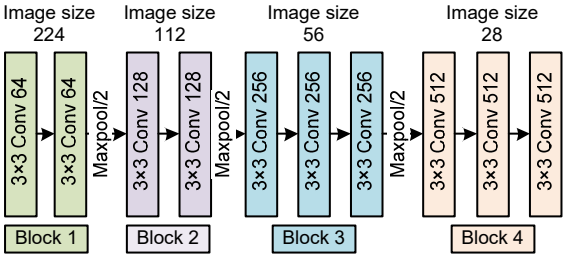



**Fig. 9 The former four blocks of VGG 16**

Fig. 9 shows the former four blocks of VGG 16, which is the first part of the whole network shown in Fig. 1. Both the first and second blocks have two convolutional layers and one maxpooling layer. The third and fourth blocks have three convolutional layers and the former has one more maxpooling layer than the latter.

Then, we train and test the datasets with "Add_Model" as shown in Fig. 1. We use a Ubuntu 16.04 computer with a four-core 4.2 GHz CPU and a GTX 1080Ti GPU. The stochastic gradient descent algorithm is applied to update the weights. The iterative solution process of the dense layer's parameter $\boldsymbol{w}$ can be found in Section 2.2.2. The batch size is 128, and the learning rate is $2\times10^{-5}$. There are 3752 training images in total, so one epoch represents 29 batches.

After 500 training batches, the training loss curve is shown in Fig. 10a. For every epoch, we save the model and obtain the testing accuracy via the testing datasets. The training and testing accuracies are shown together. The testing accuracy is 99.08% at the last epoch.

Table 2 shows the testing results of "LeNet," "AlexNet," and "VGG 16," where $P_d=N_{detect}/N_{total_boat}$ and $P_f=N_{false_alarm}/N_{total_boat}$. "bc64" means that the batch size is 64. The experimental results show that a larger batch size is useful for this classification task. Limited by the GPU's memory, we set the batch size to 128. "_Aug" means the data augmentation method, which can improve classification performance by 7.5%. Besides, the proposed multi-label method can improve performance by 1.3%. VGG 16 spends about 12.5 s to classify the TF images from dataset TFC17002.

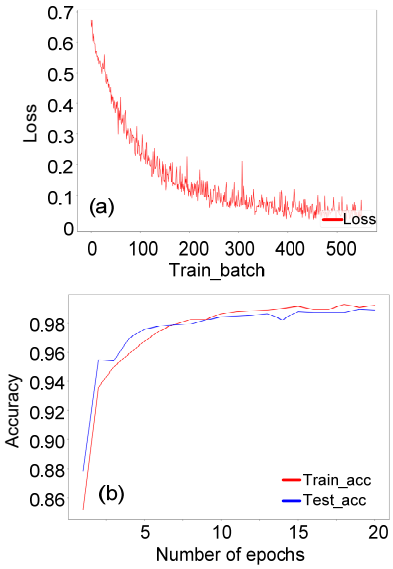



**Fig. 10 Training loss (a) and training and testing accuracies at each epoch (b)**

**Table 2 Testing results of several models**

| Model | $P_d$ | $P_f$ | Time (s) |
|---|---|---|---|
| LeNet | 0.819 | 0.188 | 6.529 |
| AlexNet_bc64 | 0.831 | 0.100 | 8.917 |
| AlexNet_bc128 | 0.863 | 0.100 | 8.767 |
| VGG_bc128 | 0.903 | 0.088 | 12.718 |
| VGG_bc128_Aug | 0.978 | 0.048 | 12.325 |
| VGG_bc128_Aug_mulabel | 0.991 | 0.006 | 12.337 |

### 3.3 Activation spectrum via DA-CCS

To search for the physical meaning of the learning system, we visualize the parameters and feature maps of the CNN. Then we can know what the network has learned. The results of activating CNN feature maps are shown in Fig. 11b.

Because of the normalization according to Eq. (3), the maximum value of matrix $\tilde{\boldsymbol{M}}_r$ is 0 dB (Fig. 11). $\tilde{\boldsymbol{M}}_r$ comes from dataset TFC17002 (range bin 32, 40.4–53.9 s). The shapes of the time-frequency spectrum of the sea clutter and the boat usually differ in time-frequency images. The red region represents the sea clutter, and the red curve represents the boat (Fig. 11a).

We make element-wise multiplication between the time-frequency image and the CAM according to Eq. (21). Then we obtain the sea clutter suppression result (Fig. 12a). Sea clutter has been suppressed

efficiently although it is quite a lot stronger than the boat as shown in Fig. 11a. According to Eq. (23), we obtain the range-Doppler map after sea clutter suppression (Fig. 12b).

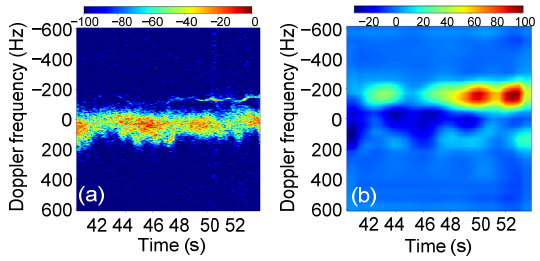



**Fig. 11 Time-frequency image (a) and class activation map (b)**

References to color refer to the online version of this figure

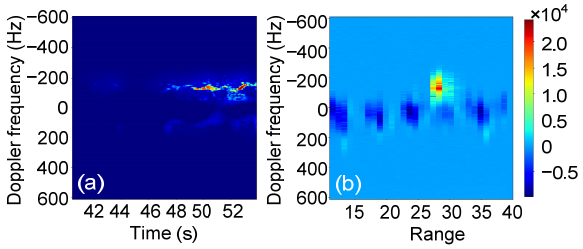



**Fig. 12 Time-frequency image (a) and range-Doppler map (b) after sea clutter suppression**

### 3.4 Analysis of detection results

In this subsection, we compare the suppression and detection performance of the proposed algorithm with that of several latest proposed methods. First, we plot one column of the CAM and the suppressed TF images. Second, detect the target with the whole dataset of TFC17002. Finally, we verify the algorithm's robustness for the Tx frequency and pulse repetition frequency with other datasets.

The results of fast Fourier transform (FFT) and ADT-SFT are shown in Figs. 13a and 13b, respectively. The Doppler frequency component with low amplitude has been suppressed by ADT-SFT. We add a Hanning window for the pulses. The results are shown in Fig. 14a. One column of the CAM is plotted in Fig. 14b.

We use the density estimation method mentioned in Section 2.2.5 for PDF and cumulative distribution function (CDF) estimation. The estimation results are accurate (Figs. 15a and 15b). The false alarm rate is $1\times10^{-4}$. The influence of the false alarm rate will be discussed later.

Yu et al. (2019) proposed adaptive moving target indication with adaptive dual-threshold sparse Fourier transform (A-ADT-SFT) for radar small boat detection. Scalar CFAR detection was employed to suppress the influence of strong clutter points. Then a subspace detector was adopted to complete target detection. Compared with ADT-SFT and A-ADT-SFT, DA-CCS has better performance. The sea clutter has been suppressed efficiently (Fig. 16b).

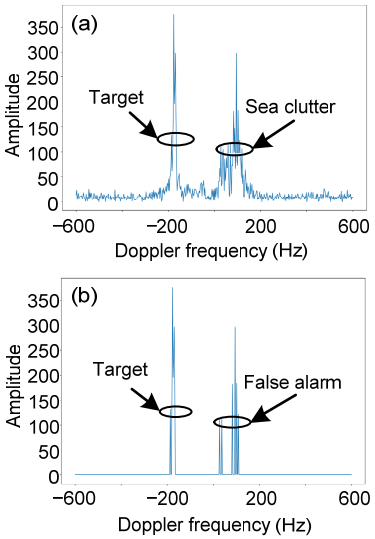



**Fig. 13 Results of FFT (a) and ADT-SFT (b)**

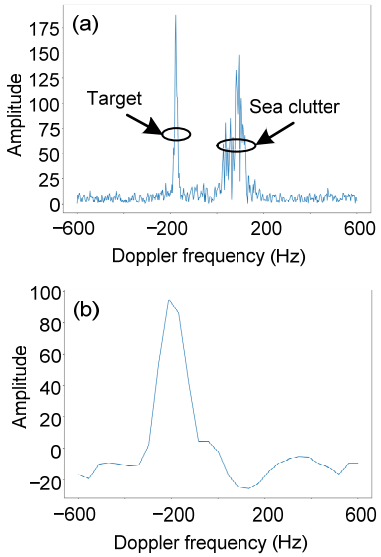



**Fig. 14 Results of adding a Hanning window (a) and one column of the class activation map (b)**

Next, we show the detection results of the DA-CCS algorithm for the whole testing dataset TFC17002. Fig. 17 shows the results of detection for the TFC17002 dataset (1–40 range bins, 0–53.88 s). There are 40 range gates in total in Fig. 17a, and the length of the pulses is 67334×4, representing about 54 s. Sea clutter is energetic, and the boat moves from range bin 20 to range bin 30. Fig. 17b presents the time-frequency images produced by the STFT.

Fig. 18a presents the detection results of CA-CFAR. The Doppler frequency of sea clutter is near zero, and there are many false alarms caused by strong sea clutter. ADT-SFT still has many false alarms, as shown in Fig. 18b, although fewer than the former's as shown in Fig. 18a.

A-ADT-SFT reduces the number of false alarms efficiently, as shown in Fig. 19a, while there are still some false alarms. We stack all of the detected range-Doppler maps together. The proposed DA-CCS algorithm has excellent detection performance as shown in Fig. 19b, with fewer false alarms.

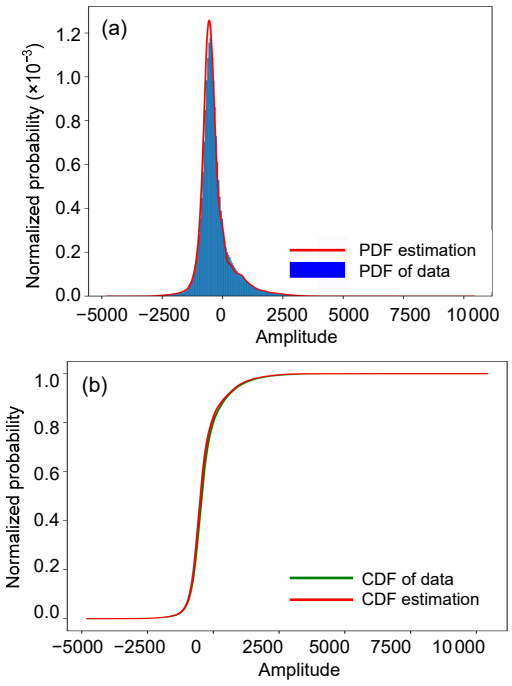



**Fig. 15 Results of PDF (a) and CDF (b) estimation**

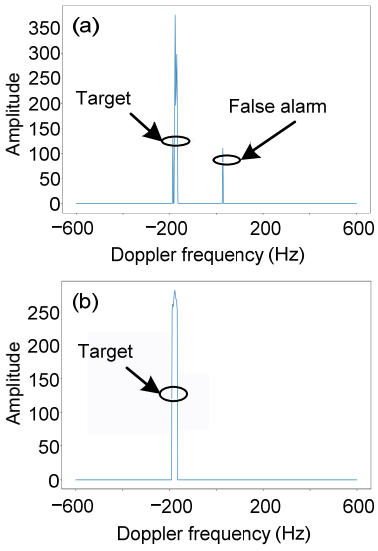



**Fig. 16 Detection results of A-ADT-SFT (a) and the proposed method (b)**

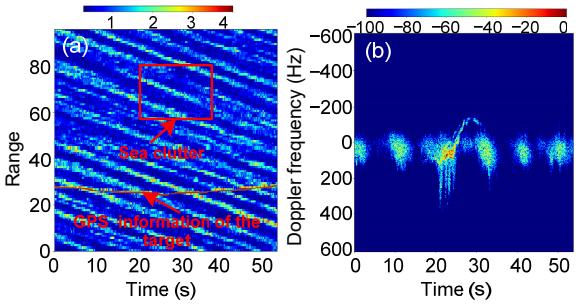



**Fig. 17 Range-pulse (a) and time-frequency (b) images**

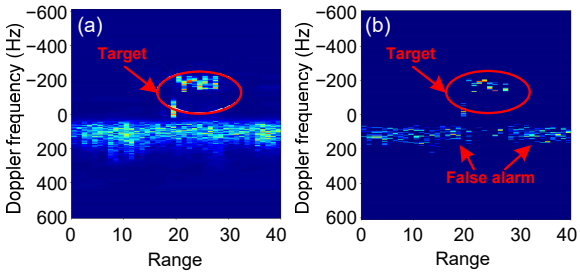



**Fig. 18 Detection results of CA-CFAR (a) and ADT-SFT (b)**

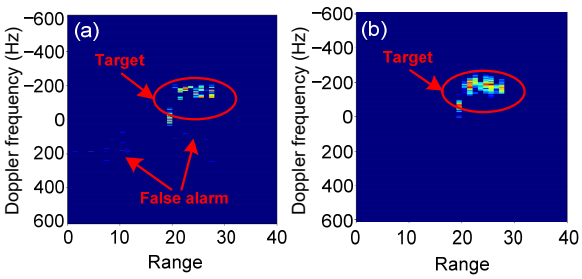



**Fig. 19 Detection results of A-ADT-SFT (a) and the proposed method (b)**

To verify the robustness of the proposed algorithm, we test it with several real datasets which represent three typical scenarios for radar target detection. In the training datasets, the distance between the target and the radar is about 3000 m. In dataset TFC15038, the distance is much longer.

It is shown that the proposed algorithm is robust to the distance between the target and the radar, according to Fig. 19 and Table 3.

**Table 3 Numbers of detected targets and false alarms**

| Dataset | Method | Number of detected targets | Number of false alarms |
|---|---|---|---|
| TFC17002 (closer target) | ADT-SFT | 93 | 15 |
| | A-ADT-SFT | 104 | 4 |
| | Proposed | 106 | 2 |
| TFC17002 (farther target) | ADT-SFT | 47 | 61 |
| | A-ADT-SFT | 83 | 25 |
| | Proposed | 103 | 5 |

Next, we test the algorithm's robustness for the Tx frequency and pulse repetition frequency. The pulse repetition frequency of dataset TFC15023 is 2.5 kHz. The Tx frequency of dataset TFA17014 is 6.9 GHz. We effect sea clutter suppression via the proposed method and obtain the suppressed range-Doppler maps.

According to the relationship between the detection threshold and the false alarm rate in Eq. (26), the detection threshold can be decided by the false alarm rate. The receiver operating characteristic (ROC) curve for the relationship between $P_f$ and $P_d$ is shown in Fig. 20.

Finally, we record the traces of the detected target and the GPS information (Figs. 21 and 22). The prediction errors are all within two range bins. These experiments verify the robustness of the proposed algorithm. We use Numpy to compute the fast Fourier transform accelerated by Numba with Python, and the compiler is Pycharm. The testing time is shown in Table 4. The detection speed is high, having the potential for real-time detection.

### 3.5 Simple discussion for application

In this subsection, we briefly analyze the method of field programmable gate array (FPGA) implementation for the DA-CCS algorithm. Applying the algorithm to an actual radar system is our next goal.

FPGA has been widely used in radar systems

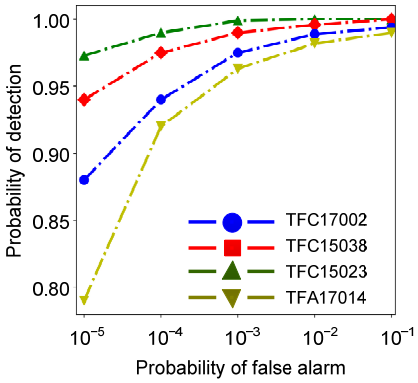



**Fig. 20 ROC curve for the proposed algorithm**

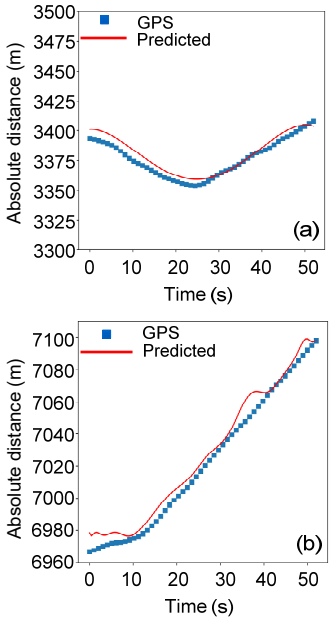



**Fig. 21 Traces of the target: (a) TFC17002; (b) farther target**

because of its small size, reliable performance, and parallel computing ability. For example, the Stratix V GX FPGA can transfer at a maximum of 12.5 Gb/s, allowing ultra-low latency and straight connections to four external 10 Gb/s small form-factor pluggable (SFP) modules.

The overall flowchart of a CNN-based heterogeneous computing system is shown in Fig. 23. There are two methods to connect the CPU with FPGA. One method is to use CPU-FPGA hybrid. The other method is to connect them through a PCI-e high-speed data transmission interface (Fig. 23).

Both GPU and FPGA are parallel computing devices. A CNN's forward propagation process is a

**Table 4 Testing time spent for target detection under several typical datasets**

| Dataset | Time (s) | | | | | |
|---|---|---|---|---|---|---|
| | Time-frequency analysis | Producing feature maps via VGG 16 | TF and RD suppression | Density estimation | CFAR detection | Total |
| TFC17002 | 14.27 | 140.87 | 56.56 | 45.52 | 0.003 | 257.223 |
| TFC15038 | 14.27 | 134.48 | 62.22 | 48.82 | 0.003 | 259.793 |
| TFC15023 | 7.71 | 103.32 | 35.73 | 45.73 | 0.003 | 192.493 |
| TFA17014 | 6.63 | 92.69 | 23.62 | 46.84 | 0.003 | 169.783 |

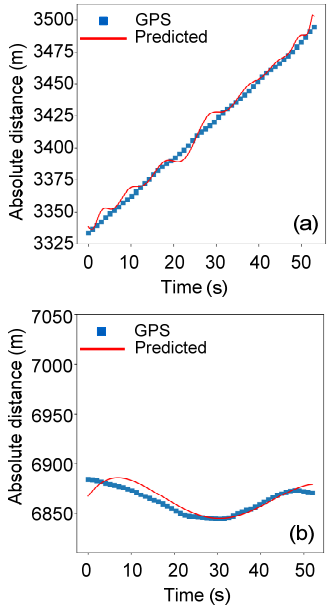



**Fig. 22 Traces of the target: (a) pulse repetition frequency is 2.5 kHz; (b) Tx frequency is 6.9 GHz**

simple and repeated operation of big data. FPGA's convolutional kernel, pooling kernel, and dense kernel are similar to those of GPU.

## 4 Conclusions

In this paper, we have proposed a dual-activation CNN based clutter suppression (DA-CCS) algorithm for radar small boat detection on the sea surface. To the best of our knowledge, it is the first time that sea clutter has been suppressed by CNN-based methods. The proposed method has excellent detection performance with high accuracy and few false alarms with measurement data.

Doppler information is one of the most important features for target detection. Non-automatic methods have been used to extract it. If we can use a CNN to extract the information directly, the proposed clutter suppression algorithm could achieve better detection performance. In the future, we will try to research automatic Doppler spectrum extraction methods and achieve FPGA implementation in real radar systems.

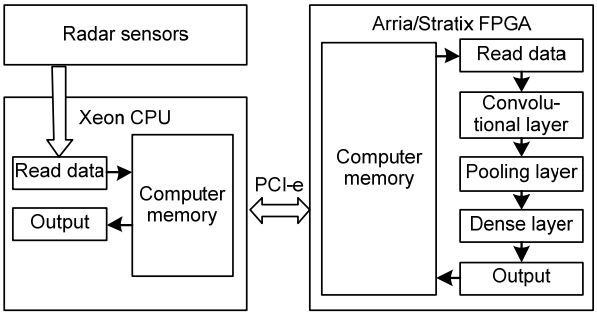



**Fig. 23 Flowchart of the FGPA implementation for the DA-CCS algorithm**

## Contributors

Zhi-yong SONG and Guan-qing LI designed the research. Guan-qing LI processed the data and drafted the manuscript. Qiang FU helped organize the manuscript. Guan-qing LI and Zhi-yong SONG revised and finalized the paper.

## Compliance with ethics guidelines

Guan-qing LI, Zhi-yong SONG, and Qiang FU declare that they have no conflict of interest.

## References

Adolfsson L, Rahm M, 2018. Machine Learning for Categorization of Small Boats and Sea Clutter. MS Thesis, Chalmers University of Technology, Göteborg, Sweden.

Angelov A, Robertson A, Murray-Smith R, et al., 2018. Practical classification of different moving targets using automotive radar and deep neural networks. *IET Radar Sonar Navig*, 12(10):1082-1089. https://doi.org/10.1049/iet-rsn.2018.0103

Conte E, de Maio A, 2004. Mitigation techniques for non-Gaussian sea clutter. *IEEE J Ocean Eng*, 29(2):284-302. https://doi.org/10.1109/joe.2004.826901

Cui XD, Goel V, Kingsbury B, 2015. Data augmentation for deep neural network acoustic modeling. *IEEE/ACM*

*Trans Audio Speech Lang Process*, 23(9):1469-1477. https://doi.org/10.1109/taslp.2015.2438544

Del-Rey-Maestre N, Jarabo-Amores MP, Mata-Moya D, 2018. Machine learning techniques for coherent CFAR detection based on statistical modeling of UHF passive ground clutter. *IEEE J Sel Top Signal Process*, 12(1):104-118. https://doi.org/10.1109/jstsp.2017.2780798

de Maio A, Foglia G, Conte E, 2005. CFAR behavior of adaptive detectors: an experimental analysis. *IEEE Trans Aerosp Electron Syst*, 41(1):233-251. https://doi.org/10.1109/taes.2005.1413759

Dong Y, 2012. Optimal coherent radar detection in a *K*-distributed clutter environment. *IET Radar Sonar Navig*, 6(5):283-292. https://doi.org/10.1049/iet-rsn.2011.0273

Farina A, Gini F, Greco MV, et al., 1997. High resolution sea clutter data: statistical analysis of recorded live data. *IEE Proc Radar Sonar Navig*, 144(3):121-130. https://doi.org/10.1049/ip-rsn:19971107

Fernández JRM, Vidal JDLCB, 2018. Fast selection of the sea clutter preferential distribution with neural networks. *Eng Appl Artif Intell*, 70:123-129. https://doi.org/10.1016/j.engappai.2018.01.008

Gilbert AC, Indyk P, Iwen M, et al., 2014. Recent developments in the sparse Fourier transform: a compressed Fourier transform for big data. *IEEE Signal Process Mag*, 31(5):91-100. https://doi.org/10.1109/msp.2014.2329131

Gini F, Greco MV, Diani M, et al., 2000. Performance analysis of two adaptive radar detectors against non-Gaussian real sea clutter data. *IEEE Trans Aerosp Electron Syst*, 36(4): 1429-1439. https://doi.org/10.1109/7.892695

Gini F, Farina A, Montanari M, 2002. Vector subspace detection in compound-Gaussian clutter. Part II: performance analysis. *IEEE Trans Aerosp Electron Syst*, 38(4):1312-1323. https://doi.org/10.1109/taes.2002.1145752

Greco M, Gini F, Rangaswamy M, 2006. Statistical analysis of measured polarimetric clutter data at different range resolutions. *IEE Proc Radar Sonar Navig*, 153(6):473-481. https://doi.org/10.1049/ip-rsn:20060045

Greco M, Stinco P, Gini F, 2010. Impact of sea clutter nonstationarity on disturbance covariance matrix estimation and CFAR detector performance. *IEEE Trans Aerosp Electron Syst*, 46(3):1502-1513. https://doi.org/10.1109/taes.2010.5545205

Guan J, Chen XL, Huang Y, et al., 2012. Adaptive fractional Fourier transform-based detection algorithm for moving target in heavy sea clutter. *IET Radar Sonar Navig*, 6(5): 389-401. https://doi.org/10.1049/iet-rsn.2011.0030

Guo Q, Yu X, Ruan GQ, 2019. LPI radar waveform recognition based on deep convolutional neural network transfer learning. *Symmetry*, 11(4):540. https://doi.org/10.3390/sym11040540

Hao CP, Orlando D, Foglia G, et al., 2014. Persymmetric adaptive detection of distributed targets in partially-homogeneous environment. *Dig Signal Process*, 24:42-51. https://doi.org/10.1016/j.dsp.2013.10.007

Hassanieh H, Indyk P, Katabi D, et al., 2012. Simple and practical algorithm for sparse Fourier transform. Proc 23rd Annual ACM-SIAM Symp on Discrete Algorithms, p.17-19. https://doi.org/10.1137/1.9781611973099.93

Herselman PL, de Wind HJ, 2008. Improved covariance matrix estimation in spectrally inhomogeneous sea clutter with application to adaptive small boat detection. Proc IEEE Int Conf on Radar, p.26-30. https://doi.org/10.1109/radar.2008.4653898

Herselman PL, Baker CJ, de Wind HJ, 2008. An analysis of X-band calibrated sea clutter and small boat reflectivity at medium-to-low grazing angles. *Int J Navig Observ*, 2008: 347518. https://doi.org/10.1155/2008/347518

Jafarzadehpour F, Molahosseini MS, Zarandi AAE, et al., 2019. Efficient modular adder designs based on thermometer and one-hot coding. *IEEE Trans VLSI Syst*, 27(9):2142-2155. https://doi.org/10.1109/tvlsi.2019.2919609

Jay E, Ovarlez JP, Declercq D, et al., 2002. Bayesian optimum radar detector in non-Gaussian noise. Proc 26th Int Conf on Acoustics, p.13-17. https://doi.org/10.1109/ICASSP.2002.5744038

Khan A, Sohail A, Zahoora U, et al., 2019. A survey of the recent architectures of deep convolutional neural networks. https://arxiv.org/abs/1901.06032

Kong SH, Kim M, Hoang LM, et al., 2018. Automatic LPI radar waveform recognition using CNN. *IEEE Access*, 6:4207-4219. https://doi.org/10.1109/access.2017.2788942

Lamont-Smith T, 2008. Azimuth dependence of Doppler spectra of sea clutter at low grazing angle. *IET Radar Sonar Navig*, 2(2):97-103. https://doi.org/10.1049/iet-rsn:20070099

Lei YM, Tian YK, Shan HM, et al., 2020. Shape and margin-aware lung nodule classification in low-dose CT images via soft activation mapping. *Med Image Anal*, 60:101628. https://doi.org/10.1016/j.media.2019.101628

Li Y, He MK, Zhang N, 2017. An ionospheric clutter recognition method based on machine learning. Proc IEEE Int Symp on Antennas and Propagation & USNC/URSI National Radio Science Meeting, p.9-14. https://doi.org/10.1109/apusncursinrsm.2017.8072861

Li YZ, Xie PC, Tang ZS, et al., 2019. SVM-based sea-surface small target detection: a false-alarm-rate-controllable approach. *IEEE Geosci Remote Sens Lett*, 16(8):1225-1229. https://doi.org/10.1109/lgrs.2019.2894385

Liu C, Wang J, Liu XM, et al., 2019. Deep CM-CNN for spectrum sensing in cognitive radio. *IEEE J Sel Areas Commun*, 37(10):2306-2321. https://doi.org/10.1109/jsac.2019.2933892

Liu J, Zhang ZJ, Yang Y, 2012. Performance enhancement of subspace detection with a diversely polarized antenna. *IEEE Signal Process Lett*, 19(1):4-7. https://doi.org/10.1109/lsp.2011.2173485

Liu NB, Xu YN, Ding H, et al., 2019. High-dimensional feature extraction of sea clutter and target signal for intelli-

gent maritime monitoring network. *Comput Commun*, 147:76-84. https://doi.org/10.1016/j.comcom.2019.08.016

Liu S, Huang WM, Zhang Z, 2020. Person re-identification using hybrid task convolutional neural network in camera sensor networks. *Ad Hoc Netw*, 97:102018. https://doi.org/10.1016/j.adhoc.2019.102018

Long J, Shelhamer E, Darrell T, 2015. Fully convolutional networks for semantic segmentation. Proc IEEE Conf on Computer Vision and Pattern Recognition, p.8-10. https://doi.org/10.1109/cvpr.2015.7298965

Lv MJ, Zhou C, 2019. Study on sea clutter suppression methods based on a realistic radar dataset. *Remote Sens*, 11(23):2721. https://doi.org/10.3390/rs11232721

Ma LW, Wu JJ, Zhang JP, et al., 2020. Research on sea clutter reflectivity using deep learning model in Industry 4.0. *IEEE Trans Ind Inform*, 16(9):5929-5937. https://doi.org/10.1109/tii.2019.2957379

Mahdi A, Qin J, 2019. An extensive evaluation of deep featuresof convolutional neural networks for saliency prediction of human visual attention. *J Vis Commun Image Represent*, 65:102662. https://doi.org/10.1016/j.jvcir.2019.102662

McDonald AM, de Wind HJ, Cilliers JE, 2010. Performance prediction for a coherent X-band radar in a maritime environment with *K*-distributed sea clutter. Proc IEEE Int Conf on Radar, p.1208-1213. https://doi.org/10.1109/radar.2010.5494436

McDonald MK, Cerutti-Maori D, 2016. Coherent radar processing in sea clutter environments, part 2: adaptive normalised matched filter versus adaptive matched filter performance. *IEEE Trans Aerosp Electron Syst*, 52(4): 1818-1833. https://doi.org/10.1109/taes.2016.140898

Pang CS, Liu SH, Han Y, 2018. High-speed target detection algorithm based on sparse Fourier transform. *IEEE Access*, 6:37828-37836. https://doi.org/10.1109/access.2018.2853180

Ritchie M, Stove A, Woodbridge K, et al., 2016. NetRAD: monostatic and bistatic sea clutter texture and Doppler spectra characterization at S-band. *IEEE Trans Geosci Remote Sens*, 54(9):5533-5543. https://doi.org/10.1109/tgrs.2016.2567598

Rosenberg L, Watts S, Greco MS, 2019. Modeling the statistics of microwave radar sea clutter. *IEEE Aerosp Electron Syst Mag*, 34(10):44-75. https://doi.org/10.1109/maes.2019.2901562

Sangston KJ, Gini F, Greco MS, 2012. Coherent radar target detection in heavy-tailed compound-Gaussian clutter. *IEEE Trans Aerosp Electron Syst*, 48(1):64-77. https://doi.org/10.1109/taes.2012.6129621

Sekine M, Musha T, Tomita Y, et al., 1983. Weibull-distributed sea clutter. *IEE Proc F Commun Radar Signal Process*, 130(5):476. https://doi.org/10.1049/ip-f-1.1983.0076

Shi SN, Liang X, Shui PL, et al., 2019. Low-velocity small target detection with Doppler-guided retrospective filter in high-resolution radar at fast scan mode. *IEEE Trans Geosci Remote Sens*, 57(11):8937-8953. https://doi.org/10.1109/tgrs.2019.2923790

Shnidman DA, 1999. Generalized radar clutter model. *IEEE Trans Aerosp Electron Syst*, 35(3):857-865. https://doi.org/10.1109/7.784056

Shui PL, Liu M, 2016. Subband adaptive GLRT-LTD for weak moving targets in sea clutter. *IEEE Trans Aerosp Electron Syst*, 52(1):423-437. https://doi.org/10.1109/taes.2015.140783

Shui PL, Shi YL, 2012. Subband ANMF detection of moving targets in sea clutter. *IEEE Trans Aerosp Electron Syst*, 48(4):3578-3593. https://doi.org/10.1109/taes.2012.6324742

Su NY, Chen XL, Guan J, et al., 2019. Deep CNN-based radar detection for real maritime target under different sea states and polarizations. Proc 4th Int Conf on Cognitive Systems and Signal Processing, p.321-331. https://doi.org/10.1007/978-981-13-7986-4_29

Trunk GV, George SF, 1970. Detection of targets in non-Gaussian sea clutter. *IEEE Trans Aerosp Electron Syst*, ASE-6(5):620-628. https://doi.org/10.1109/taes.1970.310062

Walker D, 2000. Experimentally motivated model for low grazing angle radar Doppler spectra of the sea clutter at small grazing angles. *IEE Proc Radar Sonar Navig*, 147(3):114-120. https://doi.org/10.1049/ip-rsn:20000386

Walker D, 2001. Doppler modelling of radar sea clutter. *IEE Proc Radar Sonar Navig*, 148(2):73-80. https://doi.org/10.1049/ip-rsn:20010182

Wang C, Wang J, Zhang XD, 2017. Automatic radar waveform recognition based on time-frequency analysis and convolutional neural network. IEEE Int Conf on Acoustics, Speech and Signal Processing, p.5-9. https://doi.org/10.1109/icassp.2017.7952594

Wang L, Tang J, Liao QM, 2019. A study on radar target detection based on deep neural networks. *IEEE Sens Lett*, 3(3):7000504. https://doi.org/10.1109/lsens.2019.2896072

Wang SG, Patel VM, Petropulu A, 2016. RSFT: a realistic high dimensional sparse Fourier transform and its application in radar signal processing. Proc IEEE Military Communications Conf, p.1-3. https://doi.org/10.1109/milcom.2016.7795442

Wang WP, Feng Y, Shan T, 2019. A sea clutter suppression method using improved time-frequency filtering method. *J Signal Process*, 35(2):208-216 (in Chinese). https://doi.org/10.16798/j.issn.1003-0530.2019.02.006

Ward KD, 1981. Compound representation of high resolution sea clutter. *Electr Lett*, 17(16):561-563. https://doi.org/10.1049/el:19810394

Watts S, 1996. Cell-averaging CFAR gain in spatially correlated *K*-distributed clutter. *IET Radar Sonar Navig*, 143(5):321-327. https://doi.org/10.1049/ip-rsn:19960745

Watts S, Ward KD, 1987. Spatial correlation in *K*-distributed sea clutter. *IEE Proc F Commun Radar Signal Process*, 134(6):526-532. https://doi.org/10.1049/ip-f-1.1987.0090

Weinberg GV, 2012. Suboptimal coherent radar detection in a KK-distributed clutter environment. *Signal Process*, 2012: 614653. https://doi.org/10.5402/2012/614653

Wu J, Wang T, Meng X, et al., 2010. Clutter suppression for airborne non-sidelooking radar using ERCB-STAP algorithm. *IET Radar Sonar Navig*, 4(4):497-506. https://doi.org/10.1049/iet-rsn.2009.0121

Yang H, Min K, 2019. A deep approach for classifying artistic media from artworks. *KSII Trans Int Inform Syst*, 13(5): 2558-2573. https://doi.org/10.3837/tiis.2019.05.018

Yasotharan A, Thayaparan T, 2006. Time-frequency method for detecting an accelerating target in sea clutter. *IEEE Trans Aeros Electron Syst*, 42(4):1289-1310. https://doi.org/10.1109/taes.2006.314573

Yu XH, Chen XL, Huang Y, et al., 2019. Radar moving target detection in clutter background via adaptive dual-threshold sparse Fourier transform. *IEEE Access*, 7:58200-58211. https://doi.org/10.1109/access.2019.2914232

Zhang L, You W, Wu QMJ, et al., 2018. Deep learning-based automatic clutter/interference detection for HFSWR. *Remote Sens*, 10(10):1517. https://doi.org/10.3390/rs10101517

Zhang RY, Cao SY, 2019. Real-time human motion behavior detection via CNN using mmWave radar. *IEEE Sens Lett*, 3(2):3500104. https://doi.org/10.1109/lsens.2018.2889060

Zhao JF, Jiang RK, Wang XT, et al., 2019. Robust CFAR detection for multiple targets in *K*-distributed sea clutter based on machine learning. *Symmetry*, 11(12):1482. https://doi.org/10.3390/sym11121482

Zhao JR, Wen BY, Tian YW, et al., 2019. Sea clutter suppression for shipborne HF radar using cross-loop/monopole array. *IEEE Geosci Remote Sens Lett*, 16(6): 879-893. https://doi.org/10.1109/lgrs.2018.2884507

Zhou BL, Khosla A, Lapedriza A, et al., 2016. Learning deep features for discriminative localization. Proc IEEE Conf on Computer Vision and Pattern Recognition, p.2921-2929. https://doi.org/10.1109/cvpr.2016.319